Heritage research at the PUMA beamline

S. Schöder, Katharina Müller, Laurent Tranchant, Angélique Rouquié, Pierre Gueriau, Mathieu Thoury, Emilie Bérard, Tulin Okbinoglu, Felisa Berenguer, Clémence Iacconi, et al.

Applied Physics A (2024) 130:848
https://doi.org/10.1007/s00339-024-08026-0

S.I.: SR2A - SYNCHROTRON RADIATION AND NEUTRONS IN ART AND ARCHAEOLOGY 2023

Heritage research at the PUMA beamline

S. Schöder[1] · K. Müller[2] · L. Tranchant[1] · A. Rouquié[1] · P. Gueriau[2,3] · M. Thoury[2] · E. Bérard[4] · T. Okbinoglu[1] · F. Berenguer[1] · C. Iacconi[5] · L. Robbiola[6] · T. Moreno[1] · S. X. Cohen[2] · L. Bertrand[5]

Received: 1 August 2024 / Accepted: 24 October 2024

Abstract
The PUMA beamline, created for the heritage community and accessible by all fields of science, welcomed its first users in 2019. Its optical layout uses a horizontal focusing mirror to prefocus the light emitted from the wiggler source for the experimental endstation. It provides a 5 µm × 7 µm microbeam for XRF, XAS, XRD and XEOL analysis or a wide 20 × 5 mm full field when the beam is defocused, and the KB mirrors are retracted. An extremely stable fixed-exit Si(111) monochromator is used to select the wavelength. Many experiments have been performed at PUMA, particularly in archaeology, paleontology, conservation, art history and in identifying safer conditions of irradiation for precious heritage samples. XRF analysis has been used, for example, to show the effects of the interaction of Palaeolithic ivory with soil; to identify the elemental composition of mineralized textiles and to reveal hidden morphologies of fossils.

Keywords Heritage science · Archaeology · Palaeontology · Radiation damage · Synchrotron · X-ray absorption spectroscopy · X-ray diffraction · X-ray imaging · XEOL · X-ray fluorescence spectroscopy

1 Introduction

Although the potential of synchrotron radiation for the analysis of heritage materials was recognized in the mid 1980s, the number of publications started to increase steadily at the beginning of the new millennium [1, 2]. While early work emphasized the ability to quantitatively estimate elemental content in archaeological materials by X-ray fluorescence (XRF); phase identification and quantitative structural description by X-ray diffraction (XRD) and small angle X-ray scattering (SAXS), as well as elemental speciation by X-ray absorption spectroscopy (XAS), were soon identified as significant contributions to understand the composition of archaeological and artistic materials. Paleontological work subsequently benefited from imaging capabilities both in 3D (through micro-computed tomography (µCT)) [3], later from scanning XRF, XAS and XRD [4–10] and even from X-ray Raman scattering (XRS) spectroscopy and imaging [11, 12]. To facilitate the access for these new user groups, it was decided to build both a beamline specialized for the needs of the community at the French national synchrotron light source SOLEIL, located on the Paris-Saclay campus south-west of Paris, and a support research platform, IPANEMA [13]. The goal was to offer a beamline with synchrotron techniques often used by the community, while being complementary to the portfolio of techniques already available at SOLEIL. The beamline and accompanying procedures were optimized to take into account several specific requirements of heritage materials, particularly their physico-chemical heterogeneity, their fragility, and the need to search for local information in large samples [14]. The name "PUMA" was chosen for the new beamline as an abbreviation for "Photons utilisés pour les Matériaux Anciens" ("Photons used for Ancient Materials"). The beamline opened its doors to its first users in 2019.

✉ S. Schöder
sebastian.schoeder@synchrotron-soleil.fr

1 Synchrotron SOLEIL, Saint-Aubin F-91190, France

2 IPANEMA, CNRS, UVSQ, MC, MNHN, Université Paris Saclay, Gif-sur-Yvette F-91192, France

3 Institute of Earth Sciences, University of Lausanne, Lausanne, Switzerland

4 Université Paris-Saclay, CNRS, ICMMO, Orsay F-91400, France

5 Université Paris-Saclay, ENS Paris-Saclay, CNRS, PPSM, Gif-sur-Yvette F-91190, France

6 TRACES, CNRS, UMR 5606, Université Toulouse Jean-Jaurès, Toulouse F-31000, France

Published online: 01 November 2024

PUMA is a hard X-ray beamline with a flexible design, which specializes in 2D micro-imaging with a lateral resolution of 5 to 10 µm. It allows users to create cartographies of their samples with the techniques of XRF, XAS, XRD, as well as X-ray excited optical luminescence (XEOL). Specific developments aim to reduce the dose administered to the sample while maintaining the interpretability of the data, for example by using sparse excitation imaging [15], and to take advantage of the wide full-field beam to carry out tomographic experiments. This article describes the beamline and provides an overview of the studies carried out to date at the PUMA beamline in the field of cultural and natural heritage.

2 Description of the beamline

The optical setup of the beamline is shown in Fig. 1. The source of the beamline is a 1.8 T wiggler with twenty 164.2 mm periods and a critical energy of 8.98 keV. A 300 µm beryllium window is mounted at the entrance of the beamline and acts as a filter for the low energy X-rays (< 1 keV). A set of primary slits allows the beam size to match the aperture of the optical elements.

A 1 m long elliptical mirror (CINEL) is used to focus the large emission cone of the wiggler in the horizontal direction. This mirror is installed at a fixed 1.3 mrad angle to the beam and features two bending motors for adjusting its curvature. This allows the focal distance of the mirror to change from 3 m to infinity, and is used to control the horizontal beam size at the sample position from around 2 mm to up to 20 mm. The water-cooled silicon substrate is coated with a 60 nm thick iridium layer to ensure total reflectivity of the X-rays from 4 to 60 keV.

The beam energy for the experiment is selected using a double crystal monochromator (DCM) with fixed-exit geometry in horizontal deflection (CINEL). It features two sets of crystals, Si(111) for an energy range of 4 to 23 keV and Si(220) for 20 to 60 keV, that are stacked vertically. The change between the two sets therefore consists of a simple vertical translation of the whole crystal goniometer. Due to the high heat load, the system is cooled by liquid nitrogen. The (less common) horizontal deflection geometry leads to an extremely stable setup once operating temperature has been reached, as the mechanics do not work against gravity.

A set of horizontal slits is placed between the monochromator and the final focusing optics to cut stray radiation.

The experimental setup is shown in Fig. 2. A KB mirror system, designed by SOLEIL, is used to focus the beam on the sample. It features an aperture of approximately 1 mm × 1 mmand can produce a focal spot of 5 µm (vertical) x 7 µm (horizontal). The flux in the focal spot at the sample position is around 10^{10} ph/s between 10 and 20 keV. At lower energies, the flux falls quickly due to air absorption in the experimental hutch, but can be raised by filling the KB mirror chamber and the flight tube upstreamwith helium. The two mirrors are each coated with a strip of B4C for use at energies below 10 keV and a strip of rhodium for use at high energies, up to 22 keV. A thin diamond intensity monitor at the exit of the mirror chamber measures the flux of the beam incident on the sample.

An 8-axis goniometer is used to accurately position the sample with respect to the beam and to perform scanning experiments. It consists of two base translation stages: along the direction of the beam (s) and perpendicular to it (x). This enables long movements to be made while scanning. Directly above these base stages, a 360-degree rotation axis allows the sample to be rotated around its vertical axis. The bottom translation stages can be used to position the rotation axis in the focal spot, while three additional translation stages are located above the rotation axis to allow the sample to be positioned and scanned while maintaining the focal spot on the rotation axis. All stages (PI/MICOS) are high precision stepper motors with optical encoders featuring

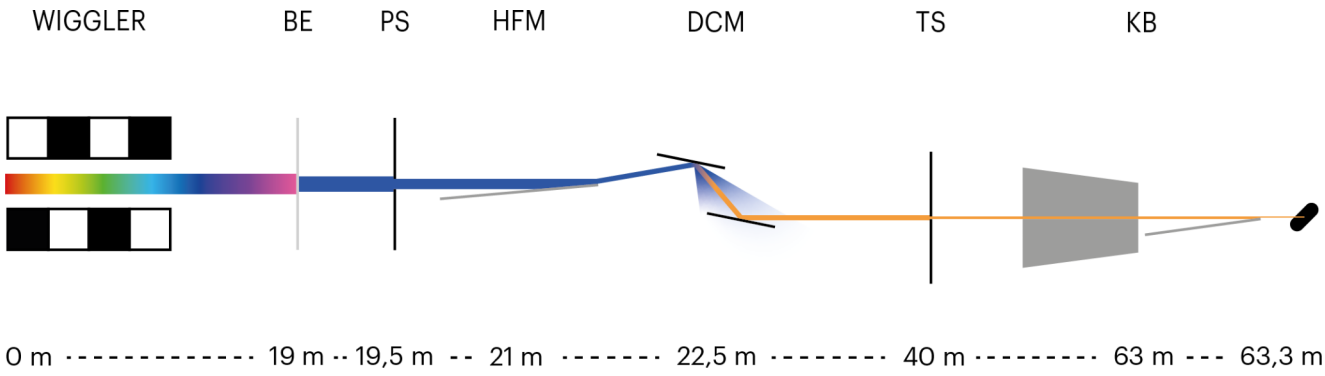

Fig. 1 Optical layout of the beamline. The source of the beamline is a wiggler. A beryllium window (BE) filters the low energy part of the beam. The primary slits (PS) match the beam size to the optical aperture of the beamline. A horizontal focusing mirror (HFM) is used to focus the beam on the tertiary slits (TS) to prefocus for the KB mirror system (KB). The energy selection is done with a double crystal monochromator (DCM)

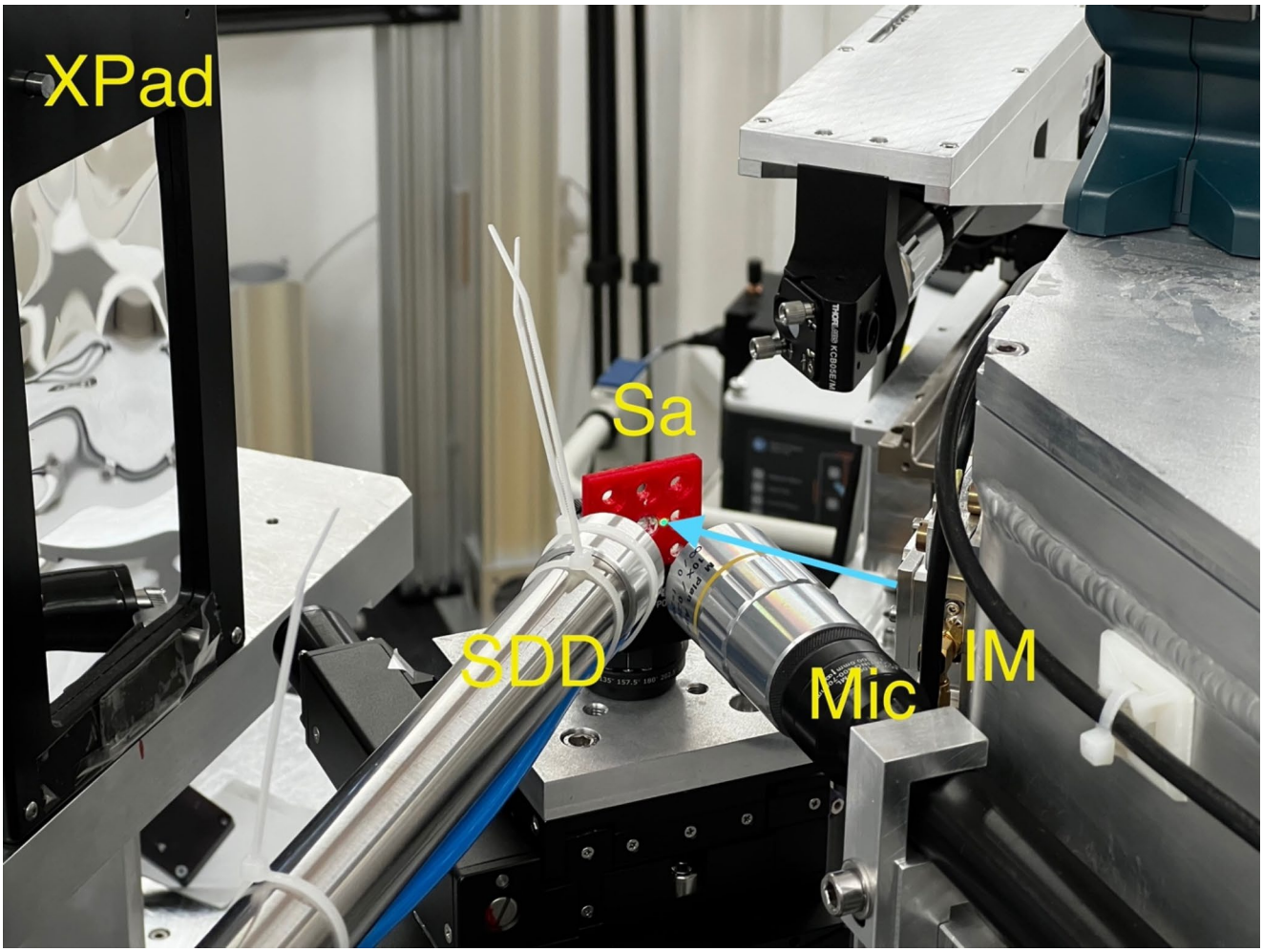

Fig. 2 Photo of the experimental setup. To the right of the image the chamber of the KB mirror can be seen. The incident X-ray beam (blue arrow) exits the chamber by passing an intensity monitor (IM) and is focalized on the sample (Sa). Here, a 3D printed holder for pellets is shown. Fluorescence from the sample can be detected with the silicon drift detector (SDD). Diffraction patterns can be collected in transmission geometry with the Xpad (Xpad) hybrid pixel detector on the far left. Lastly, XEOL signals can be analysed with the microscope (Mic), which is also used to align and monitor the sample during irradiation

50 nm resolution. Samples can be scanned up to 20 mm (vertical) by 30 mm (horizontal). Finally, two tilt stages allow the sample to be rotated by ±5° around the horizontal rotation axes. A kinematic mounting system (Thorlabs) ensures accurate and repeatable positioning of the sample. This set up is ideal for samples of sub-millimetric to centimetric size, weighing less than 1 kg.

For large, flat samples, such as fossils and manuscripts, the tilt stages can be removed to make space for larger scanning stages. This allows analysis of samples weighing several kilograms for an area of up to 100 mm (vertical) x 150 mm (horizontal).

The SOLEIL acquisition software enables point-by-point scans and high-speed continuous mapping (FLYSCAN) [16]. A silicon drift detector (SDD, Rayspec) with 80 mm^2 collimated area is placed at 90° to the incident beam and is used to collect the fluorescence signal of the sample for X-ray fluorescence spectroscopy (XRF) and X-ray absorption spectroscopy (XAS). An Xpad hybrid pixel detector (ImXPAD) is placed behind the sample on a separate detector table and used to record X-ray diffraction patterns (XRD) in transmission mode.

For typical microbeam scanning experiments, the sample surface of interest is placed in a 45° geometry with respect to the incident beam. This configuration enables the use of a video-microscope (SOLEIL) with a high-quality scientific camera (Orca, Hamamatsu) to constantly image the sample surface. After aligning the microscope on the beam focal spot, the sample can be positioned with micrometric precision for the experiment without need of irradiating it, which is of great importance for radiation sensitive samples [3, 4]. This microscope also allows the sample to be observed during irradiation, and can therefore be used to monitor any anomalies such as radiation effects or light emission under

X-ray irradiation (X-ray excited optical luminescence, XEOL). A LED illuminator canproject light onto the sample from the red to the UV range. The camera is equipped with a filter wheel to select the wavelength ranges that can be observed, making it thus capable of UV luminescence analysis. In addition, it is possible to divert the microscope signal with a switchable mirror towards a fiber optic that connects to an optical spectrometer (ANDOR), for analysis of the spectrum with a highly sensitive Orca Quest camera system (Hamamatsu), ideal for XEOL spectroscopy.

3 Examples of research

3.1 Published studies

As the name implies, PUMA was created primarily with heritage research in mind. Nevertheless, the beamline is open to all scientific fields and has been used by different scientific communities outside the heritage field, for example to analyze polluted soils [17], materials used for decontamination of industrial wastewater [18], micro-meteorites [19] or detectors [20]. However, a major part of both user and in-house research is done in the heritage field and will be discussed in more detail here.

3.1.1 Archaeology

Archaeological projects done at PUMA concern a wide variety of materials, particularly ceramics, metals, glasses, pigments and biomaterials, such as bone and ivory. Most projects use XRF to determine elemental fingerprints of the samples. This is particularly important for provenance studies, where the measured data can be compared to references from other objects or from raw materials (e.g., ores) of known origin. XANES is often used, in addition, to determine the oxidation state and the mineralogic phase under which the element is found.

For example, Gianoncelli et al. [21, 22] have applied these techniques to Greek ceramic artefacts from an excavation in Gella (Italy). They established that ceramics found within the same excavation but are attributable to different regional workshops do indeed exhibit important elemental differences in both the clay body and the glaze. Furthermore, the authors have shown that, in addition to elemental composition obtained from XRF, knowledge of the crystalline and amorphous phases in the sample via XANES can be advantageous for the comparison of ceramic artefacts.

Tapia et al. combined lab-based confocal XRF with synchrotron radiation XRF mapping to study red coloring matter found in prehistoric cave paintings from the *La Garma* and *Altamira* Caves in Spain. The team was able to define criteria for distinguishing between the wall support and the drawings, and was also able to better characterize the red pigments [23, 24]. XRF analysis performed by the same group on a sample taken from a drawing of a bison at the *Font-de-Gaume* cave, France, allowed to determine the place of origin of the sample within the cave and the composition of the pigments used for the local painting of a bison [25].

Moutsiou et al. used XRF on raw picrolite samples taken from various locations in Cyprus to demonstrate that XRF fingerprinting could help to provenance picrolite artefacts [26].Palaeolithic mammoth ivory samples were analyzed with μXRF and XANES by Tranchant et al. to improve the differentiation between biogenic and diagenetic elements and thus define markers of origin. This study will be discussed in more detail later.

3.1.2 Paleontology

While the use of synchrotron radiation to reconstruct the internal anatomy of fossils in three dimensions using computed tomography began in paleontology in the early 2000s, the use of XRF mapping is more recent. The usefulness of this technique was first demonstrated by Bergmann et al. at SSRL, Stanford [4]. Since then, XRF mapping of fossils has become an important axis of research at PUMA.

The usefulness of elemental maps can be twofold: as a wide range of minor to trace elements commonly replace atoms in specific tissues, their distribution can be used to enhance anatomical visualization and their abundance to document fossilization processes. Of primary interest for anatomical studies are transition metals such as Fe, Cu and Zn, which can be part of biomolecules with specific biological functions (e.g. oxygen carriers, pigmentation) and have the potential to be preserved for millions of years within various fossils (e.g. [6, 27–28]). Heavy elements such as As, Pb, Sr and Y, which offer important information depth (typically up to 200–400 μm in shales, calcium phosphates and carbonates), can unveil anatomical features hidden under the sedimentary matrix covering the specimen or under other tissues [7, 29, 30]. For example, in a recent work by Laibl et al. [31], the distribution of arsenic obtained from XRF scanning at a 5 μm lateral resolution unveiled the morphology of thoracic appendages hitherto invisible in a juvenile trilobite specimen from Morocco.

Another advantage is the local characterization of the major-to-trace elements in an elemental inventory of the various tissues which allows paleontologists to document remnants of the original chemistry of fossil organisms and/or their taphonomic history (i.e. fossilization pathway). For instance, in a first attempt to decipher the taphonomic history of a newly discovered Ordovician fossil site from South

France, Saleh et al. [32] used XRF and XANES to establish that the fossils are essentially made up of a layer of Fe(III) oxide/hydroxide crystals, varying in thickness and containing traces of metals. The distribution of other elements, notably manganese and arsenic, strongly suggests that iron (hydr)oxides do not represent the original mode of preservation of these fossils, but rather result from more recent alteration processes, as demonstrated for other contemporary deposits.

The design of the PUMA beamline has also allowed Saucède et al. to demonstrate that some fossil tissues do not only show optical luminescence when irradiated by ultraviolet (UV) light, but also when irradiated by X-rays (XEOL) [33]. This behavior is highly specific to certain mineralogies and molecules, but might open the possibilities for new developments in the analysis of fossils.

The analysis of fossils at the PUMA beamline will be discussed in more detail later in the article using specific examples.

3.1.3 Conservation

Conservation science deals with artefacts, typically from museum collections, that are undergoing some physical (e.g., cracking) or chemical (e.g., discoloration) change. Most of the samples analyzed at PUMA in this field display discolorations that are due to chemical reactions taking place at a very slow speed. These changes are often very localized, a common example being pigments in heterogeneous paint layers. Thus, a probe is needed that can determine chemical information, such as the oxidation state or the coordination number of target atoms, with microscopic resolution.

XAS enables this by scanning the energy of an incident X-ray microbeam across the absorption edge of an element, revealing information about that element only. This highly specific information is extremely useful in heterogeneous samples. For example, the degradation state of smalt pigments was revealed by XANES in Jacopo Bellini's *Madonna of Humility*, one of the earliest paintings where smalt was used as a pigment [34], and in the painting *Woman doing a Libation* or *Artemisia* (anonymous) [35].

X-ray diffraction can be used to determine corrosion products in a sample and thus reveal reaction pathways. This can lead to the identification of compounds, which play an important role in these reactions and whose presence degrades the lifetime of an artefact. Clerici et al. [36] highlighted for example the important role of chlorine corrosion products found in debris from the Basilica of St. Francis of Assisi, which had been damaged in an earthquake.

3.1.4 Safer conditions of irradiation

Radiation effects concern all fields of research. However, ensuring safer conditions of irradiation is particularly important to safeguard heritage artefacts [37, 38]. As the artefacts investigated are unique and often precious, special care must be taken to ensure that they are preserved for future generations. This also includes future scientists who may find out that certain artefacts can no longer be studied because they have been excessively altered by previous experiments, even at a local scale. Research on radiation damage has therefore been an important axis on the PUMA beamline since the start of user operation.

Gimat et al. have investigated the link between radiation and depolymerization of cellulose fibers in model and historical papers. They showed a linear correlation between radiation dose and the number of cellulose scissions coupling controlled irradiation with size-exclusion-chromatography (SEC) [39] on pure cellulose model papers. In addition, they showed that UV luminescence is a powerful technique for tracking effects post-irradiation, and that the luminescence of the irradiated areas of paper continued to increase over the year following the irradiation of the sample, while the non-irradiated parts showed no luminescence. They also investigated the role of additives and the behavior of artificially aged and historical papers under irradiation [40].

Electron paramagnetic resonance (EPR) is a powerful tool to detect radicals created in solid media. Godet et al. [41] used this technique to identify and track radicals created in Egyptian blue and green pigments during irradiation. They showed that Egyptian green pigments were more radiation-sensitive than blue ones, which was attributed to the radiation sensitivity of the predominant amorphous phase in Egyptian green pigments. In addition, Egyptian green showed clear color changes under irradiation, while no such effect was observed for Egyptian blue.

3.2 Detailed studies

After reviewing results that were published by users and scientists of the PUMA beamline, three studies of in-house research will be presented in more detail in the next paragraphs. These examples have been selected to show the breadth of the research carried out by the scientific team of the beamline and its associates.

3.2.1 Paleolithic Ivory

Mammoth ivory was used to manufacture the first jewelry and figurative art objects known, which provide valuable clues to human life in prehistoric times [42–44].

Prehistorians are investigating issues such as the availability of ivory as a raw material in the various regions and the resulting procurement strategies. These questions can be answered by analyzing geochemical markers in Palaeolithic ivory that are characteristic for its origin. The aim of this study was to identify trace elements as site-specific markers associated with mammoth habitat (endogenous elements) and to determine the chemical changes in the ivory composition over time in relation to local storage conditions, such as the uptake of exogenous elements.

A total of 12 archaeological ivory samples coming from several prehistoric sites have been analyzed at the AGLAE accelerator using PIXE/PIGE techniques and elements such as Zn, Br and Sr have been identified as endogenous elements while elements such as F, Fe or Mn as exogenous elements [45]. Tranchant et al. showed that XRF analyses at the PUMA beamline allow additional trace elements to be mapped (e.g. Rb, Y, Pb) due to the higher sensitivity for heavier elements ($Z > 19$). PIXE/PIGE analyses at AGLAE are more suitable for the analysis of elements lighter than Ca and are more surface sensitive than XRF because of the higher information depth of the X-ray fluorescence signal [46]. In addition, PIXE/PIGE analyses are routinely combined with RBS measurements at AGLAE, enabling the determination of elements up to C. This shows the interest of combining analyses at both facilities to obtain a more complete chemical characterization of ivory (organic and inorganic parts).

The investigations on the PUMA beamline helped to improve the distinction between endogenous and exogenous elements in ivory previously obtained at AGLAE. Two-dimensional XRF mappings of trace elements from Ti to Pb enabled visualization of their spatial distribution over an area of a few 100 µm × 100 µm (see Fig. 3a). A heterogenous distribution is characteristic of an exogenous element (Ti, Mn, Fe, Rb, Y, Ba, Pb) and a homogenous one characteristic for an endogenous element (Zn, Br, Sr). Cu is a potential new endogenous marker. Moreover, semi-quantitative evaluation of the 2D mappings obtained for the whole corpus of artefacts from Hohle Fels was conducted (Fig. 3b). This analysis provided supplementary information on the discrimination between endogenous and exogenous elements [47].

In addition, XANES measurements were carried out for selected elements. Figure 4 presents Mn K-edge and Sr K-edge XANES spectra obtained for the same ivory sample as in Fig. 3a. We compared the obtained spectra with the most appropriate reference samples (hollandite ($Ba(Mn4+6Mn3+2)O16$) for Mn and fluorapatite (FAp) for Sr). Hollandite is associated with sedimentary deposition [48], which is consistent with the limestone containing location where the Hohle Fels archaeological samples were found [49]. The Mn oxide observed on this sample can be identified as hollandite which precipitated during diagenesis. This consideration again confirms the exogenous character of Mn.

The chemical state of Sr is similar to Sr in FAp, which is not surprising as the structures of FAp and ivory are very close (Sr incorporates into both bone and FAp at Ca sites). The inorganic part of ivory consists of carbonated hydroxyapatite, which tends to undergo chemical alterations due to bioerosion processes in FAp [50].

3.2.2 Mineralized textiles

Iacconi et al. [45–46] studied archaeological textiles from the Iron Age site of Creney-le-Paradis (Aube, France), preserved in a "mineralized" form. The results obtained at PUMA provided chemical and mineralogical information, which complemented the morphological data collected with synchrotron computed tomography at micro and nano scales, on the PSICHE and ANATOMIX beamlines of SOLEIL, respectively. Two main objectives were pursued in identifying the spatial distribution of elemental composition, chemical speciation and mineral phases present in the samples: (1) to identify the nature of copper corrosion products formed on the textile, and (2) to collect information on the metal substrate, in addition to laboratory SEM-EDX analysis. To this end, µ-XRF, µ-XRD and µ-XAS data were collected at PUMA. XRF surface scans were performed at a 10 to 25 µm step scan and at an excitation energy of 19.7 keV (100 ms / pixel) to obtain distribution maps of the elements on entire mineralized textile fragments. On specific points of interest, XANES spectra collected at the Cu and As K edges, between 8.90 et 9.25 keV and 11.931 and 12.50 keV, respectively, with a beam size of 5 µm × 7 µm (1s per energy step), a XANES map was acquired at the As K-edge, between 11.931 and 12.50 keV (exposure time 500 ms per energy point). Energy calibration for XAS was performed by using a Cu metallic foil and setting the first inflection point of the edge to 8979 eV. The results confirmed that the metal substrate, visible over a few hundred µm on a fragment edge, is a tin bronze containing minor (As, Sb, and Ag) and trace (Fe, Pb, possibly Ni, and Au, $Bi < 0.1$ wt%) elements (Fig. 5). In corroded areas, on the surface and in corrosion products, typical elements from archaeological buried soil were also detected: Mg, Al, Si, P, Cl, K, Ca and Ti. Common trace elements in ancient copper base alloys are As or Sb with Ag often related to "grey copper" ores (also anciently named fahlerz). These copper sulfide minerals could be related to different tennantite-Cu or tetrahedrite mineral series, as recently defined via a new nomenclature for tetrahedrite group [53, 54]. However, very little Fe and no S and Zn were detected both by EDS and by

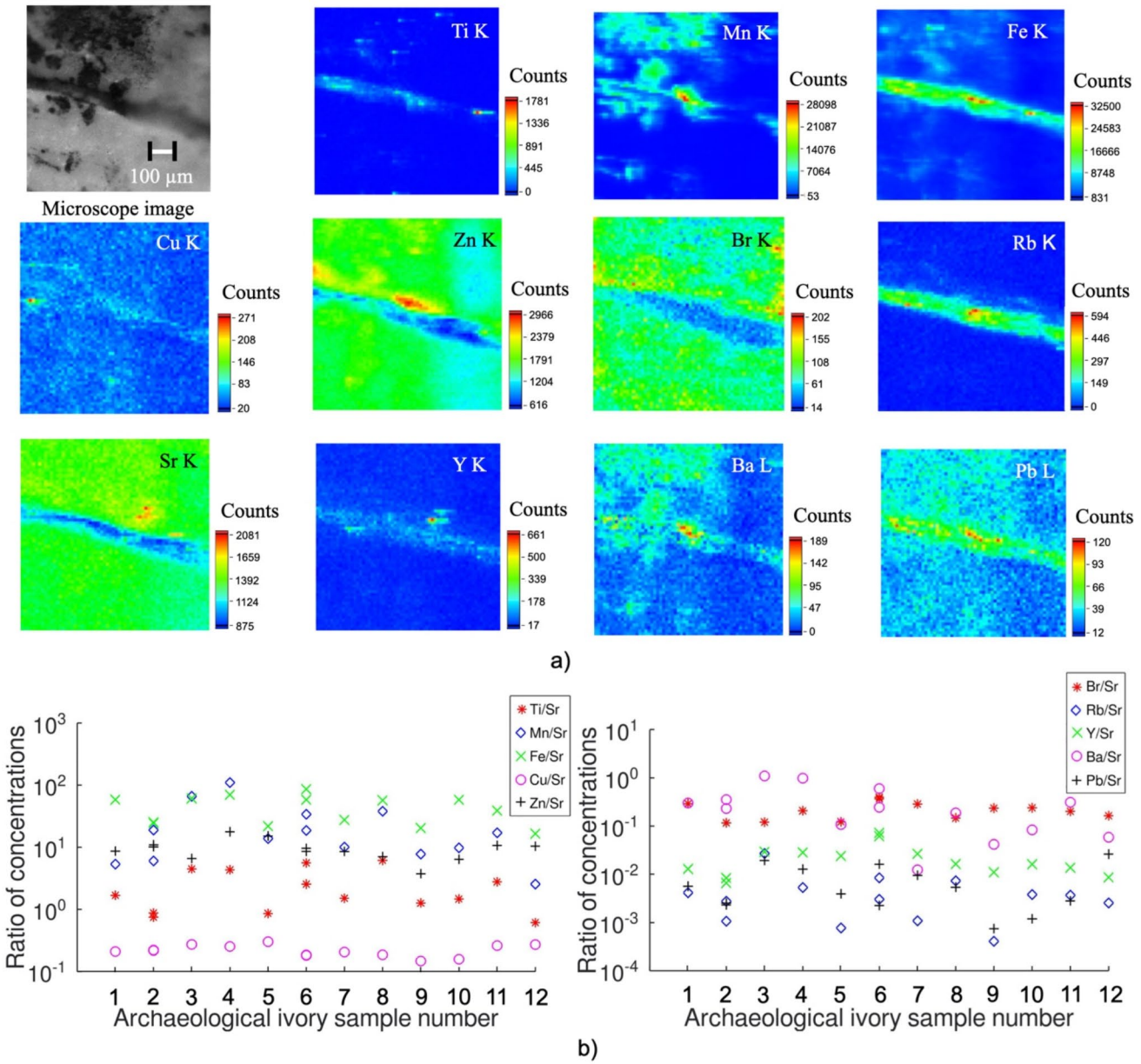

Fig. 3 (a) XRF mappings of the archaeological ivory sample AI-HF-03 [46]. (b) Normalized concentrations of trace elements regarding to Sr for the 12 studied archaeological ivory samples of the Hohle Fels cave. The plot on the left shows the results for Ti, Mn, Fe, Cu and Zn, the plot on the right for Br, Rb, Y, Ba and Pb. Results of trace elements are classified by increasing atomic number [47]

XRF in the alloy. Thus, the hypothesis of the use of fahlerz type ("grey copper"), mixed copper sulphide with mainly Sb (ref. mineral: tetrahedrite) and/or As (ref. mineral: tennantite) is not manifest. Copper(I) oxide (ref. phase: cuprite, Cu_2O) was not identified on the textile surface. Extracted individual fibers were mounted vertically on a metal support (Huber model 1002-18MS; height: 1.3 cm; diameter: 0.31 cm) held in place with glue. The mount was then attached to a Huber 1005 goniometer head (Huber Diffraktionstechnik, Rimsting, Germany) which is compatible with the micro and nano-tomography setups at ANATOMIX, where the samples had been investigated beforehand. They were analyzed using XRD (beam diameter: 10 µm, acquisition time: 1s/point) at an energy of 20 keV to maximize the transmission of the samples. The combined XRF and XRD results confirmed that the two main mineral corrosion products were basic copper(II) carbonates (ref. minerals: malachite $Cu_2(OH)_2CO_3$ and azurite $Cu_3(OH)_2(CO_3)_2$).

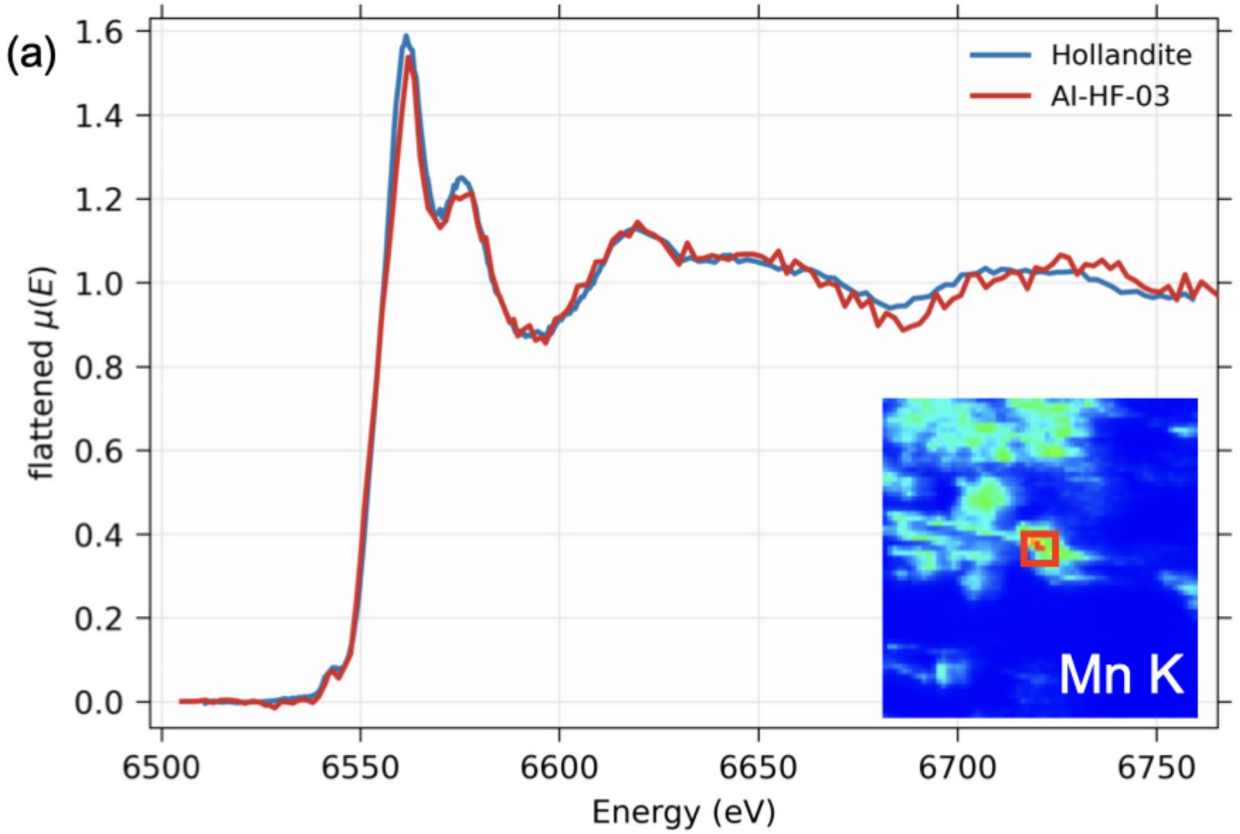
(a)
Hollandite
AI-HF-03
flattened μ(E)
Energy (eV)
Mn K

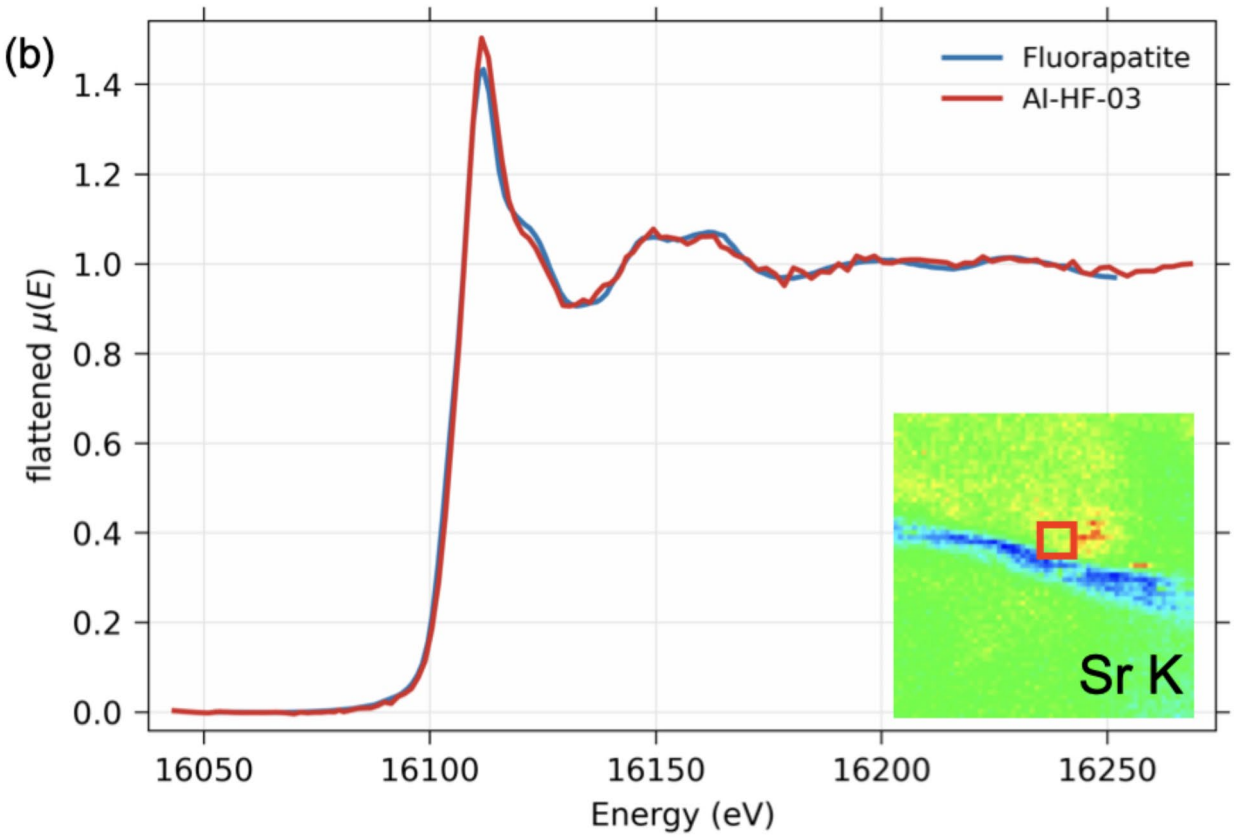
(b)
Fluorapatite
AI-HF-03
flattened μ(E)
Energy (eV)
Sr K

Fig. 4 Mn K-edge (a) and Sr K-edge (b) XAS spectra of the sample AI-HF-03 compared with hollandite for Mn and FAp for Sr. Mn K-edge and Sr K-edge XRF mappings in the inserts show the analyzed spot for XAS (10 µm x 5 µm) with a red rectangle. XAS data were treated using XAS viewer software (Larch). We corrected the self-absorption for the hollandite XANES spectrum

3.2.3 Fossils

We further illustrate here the potential of the PUMA beamline for palaeontological studies through two additional case studies: the XRF mapping and XAS spectroscopy of a branchiosaurid amphibian from the Late Carboniferous (ca. -300 Myr) of Montceau-les-Mines, France (Fig. 6A–D), and the XEOL imaging of a shrimp from the mid-Cretaceous (ca. -100 Myr) of Jbel oum Tkout, Morocco (Fig. 6E–G).

The fossil branchiosaurid amphibian appears extremely flattened, with only the body outline, some scales, and a few limb bones preserved in an ovoid sideritic ($FeCO_3$) concretion (Fig. 6A). This fossil, however, is actually three-dimensionally preserved beneath the splitting surfaces. The study of this pluri-centimetric fossil is a case example of the application of the larger scanning stages (Fig. 6B), which can be used to accommodate a single large sample or several smaller samples for multi-acquisitions. Here, hitherto invisible vertebrae, pelvic, limb and skull bones are unveiled by the distributions of calcium and yttrium (Fig. 6C). The overlay of the calcium and yttrium distributions presented in Fig. 6C illustrates how the XRF signal escapes from different depths depending on atomic weight: the Ca signal is subsurface whereas signal from Y K-lines can escape from a depth of a few 100 µm in fossils. Due to its preferential substitution for Ca in calcium phosphates (apatite group minerals and bone), the µ-XRF mapping of yttrium represents an excellent proxy to reveal hidden skeletal features in flattened vertebrate fossils [7, 29]. Note that XRF of strontium, which also substitutes for Ca in calcium phosphates, yields similar results in many cases, yet Sr similarly substitutes for Ca in calcium carbonates resulting in the absence of contrast when fossils are preserved on limestone or siderite as for the Montceau-les-Mines amphibian [29]. In addition to the revealed skeletal features, the Y distribution also uncovers another previously invisible structure distinct from the amphibian remains: a surrounding halo that decreases in intensity as it extends away from the fossil. While this halo does not provide information about the anatomy of the fossil, it documents previously unknown processes that occurred during the formation of the concretion, thereby contributing to the understanding of the fossil's taphonomic history. Interestingly, there is no overlap of Ca and Y in the halo, which indicates that its composition is not bone, but something else. The speciation of yttrium in the halo and fossil was investigated using XAS at the yttrium K-edge. Collected spectra confirmed that Y in bone is present as yttrium substituting for Ca in fluorapatite, and that the speciation of Y in the halo is different (Fig. 6D), corresponding to a form that remains to be identified in future studies.

The Cretaceous shrimp is dorso-ventrally flattened, with only the cephalothorax (i.e. head) and the first two abdominal segments visible (Fig. 7A; see Fig. 4f in [8] for a schematic anatomical reconstruction). It has been preserved through phosphatization, including finely replicated cuticular and muscular features [7, 55], and as such emits strong luminescence when illuminated by UV light (Fig. 7B). Using the band-pass multispectral XEOL imaging capabilities of the PUMA beamline, we collected XEOL emissions in the yellow, red and near infrared domains under 12.5 keV irradiation for the anteriormost part of the specimen. The false color overlay of the emissions in these domains resolves the different anatomical features at high resolution, while also exhibiting luminescence contrasts between different regions (Fig. 7C). These contrasts reveal variations in probed depth and composition, with the latter offering promising potential for further documenting the taphonomic history of the fossil.

4 Conclusion and outlook

The instrumentation of PUMA is constantly evolving to make use of innovative technologies and to adapt its capacities to the needs of its user community.

In the next years, the replacement of the wiggler with a U20 undulator source is planned, which should increase the flux in the whole energy range by around an order of magnitude, allowing users to measure more samples with higher statistics and/or larger maps. The focal spot size as well as the detection limits for all elements will also be significantly improved.

Tomography

While currently only microbeam experiments are proposed to users at PUMA, the development of an endstation for computed microtomography (CT) experiments has been an integral part of the design process. This endstation will provide a large field of view of approximately 5 mm (vertical) × 20 mm (horizontal), access to high energies up to 60 keV, and the use of a white beam. This setup will be optimized for µCT imaging of organic to moderately dense samples. The maximum sample size that can be imaged is expected to be up to about 35 mm wide and several centimeters high, achieved by extending the field of view horizontally through off-center positioning of the rotation axis and vertically by recording a series of acquisitions with vertical sample movement.

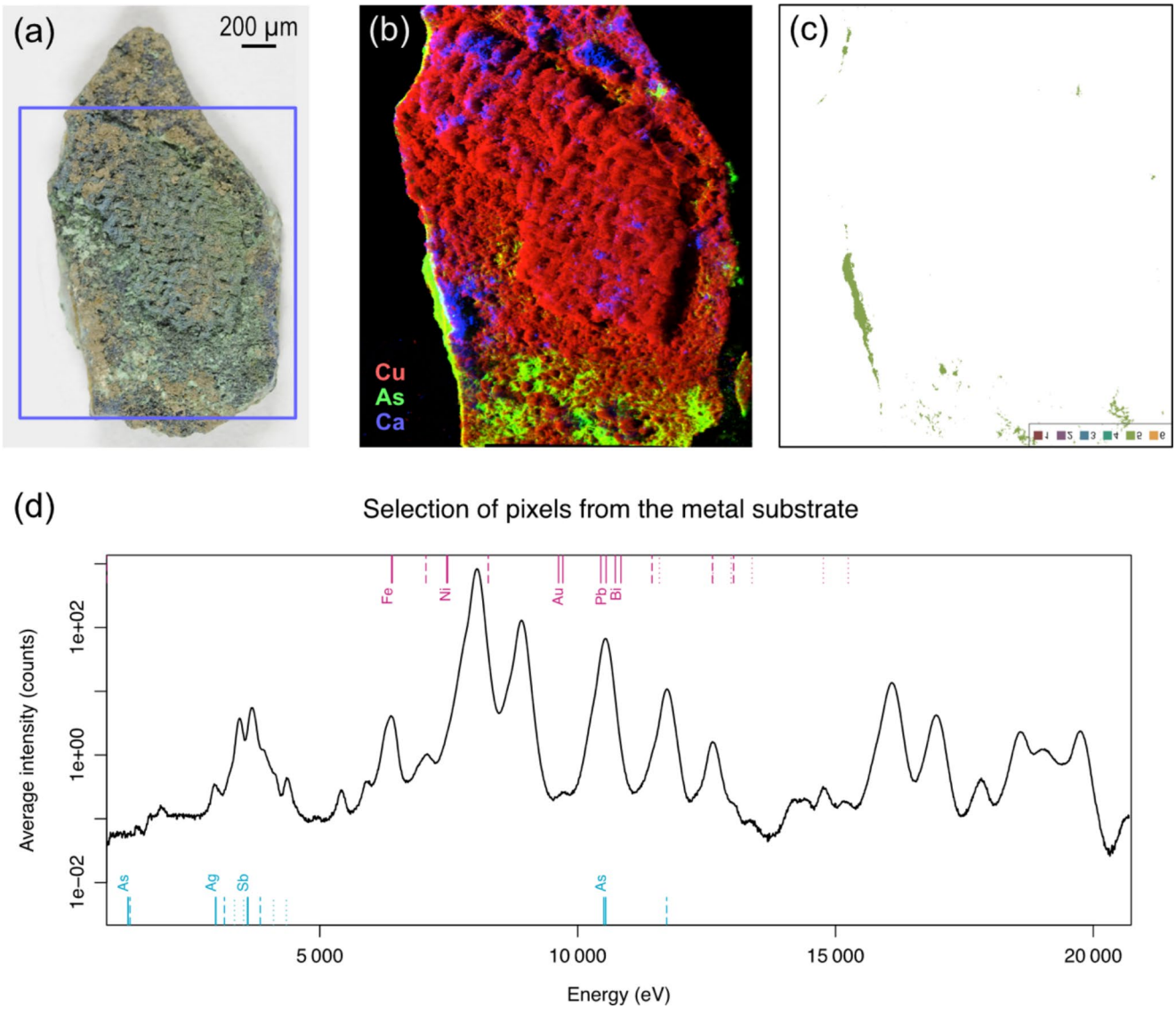

Fig. 5 Analysis of a mineralized textile sample from the Iron Age site of Creney-le-Paradis (Aube, France). (a) Macrophotography of the surface of the sample showing a copper slab covered with altered textiles; the corrosion phases consisting mainly of basic copper(II) carbonates. (b) False color XRF raster scan RGB image of the area outlined in blue in (a), showing the distribution of copper (red), arsenic (green) and calcium (blue). The arsenic is confined to the corroded copper plate and is visible on the extreme left and bottom of the samples, corresponding respectively to the fractured edge and an area with abraded textiles. (c) Image showing the pixels identified as part of the copper plate from segmentation using k-means after normalization and standardization of the spectral data. (d) Identification of peaks in the mean spectrum corresponding to the copper slab in (c), see text for discussion

A prototype has been made and several test experiments, currently only using monochromatic incident beam, have shown the potential of such a station for PUMA. For instance, the first dataset collected on a real sample at PUMA and 3D rendered is an insect trapped in Eocene (ca. -45 Myr) amber from Poland (Fig. 7D–F). A notable feature of the prototype developed at PUMA is its use of a high-definition camera, which achieves submicrometric voxel sizes for samples up to several centimeters wide, with a typical ratio of 10,000 to 15,000 between the field of view and the reconstructed voxel edge-size. This is the feature of this experimental end station, which proved essential in characterizing long distance characteristics of micro-pore networks in archaeological ceramic sherds. Using this setup, Coli et al. [56] explored the use of high-definition tomography, typically imaging a 40 mm diameter ceramic sherd at 5 µm voxel resolution, to document ceramic *chaine opératoire* by characterising its pores and crystallite grains networks.

Upgrade

SOLEIL is currently preparing a challenging upgrade program to convert its accelerators into a 4th generation storage ring [54]. The installation is currently expected to

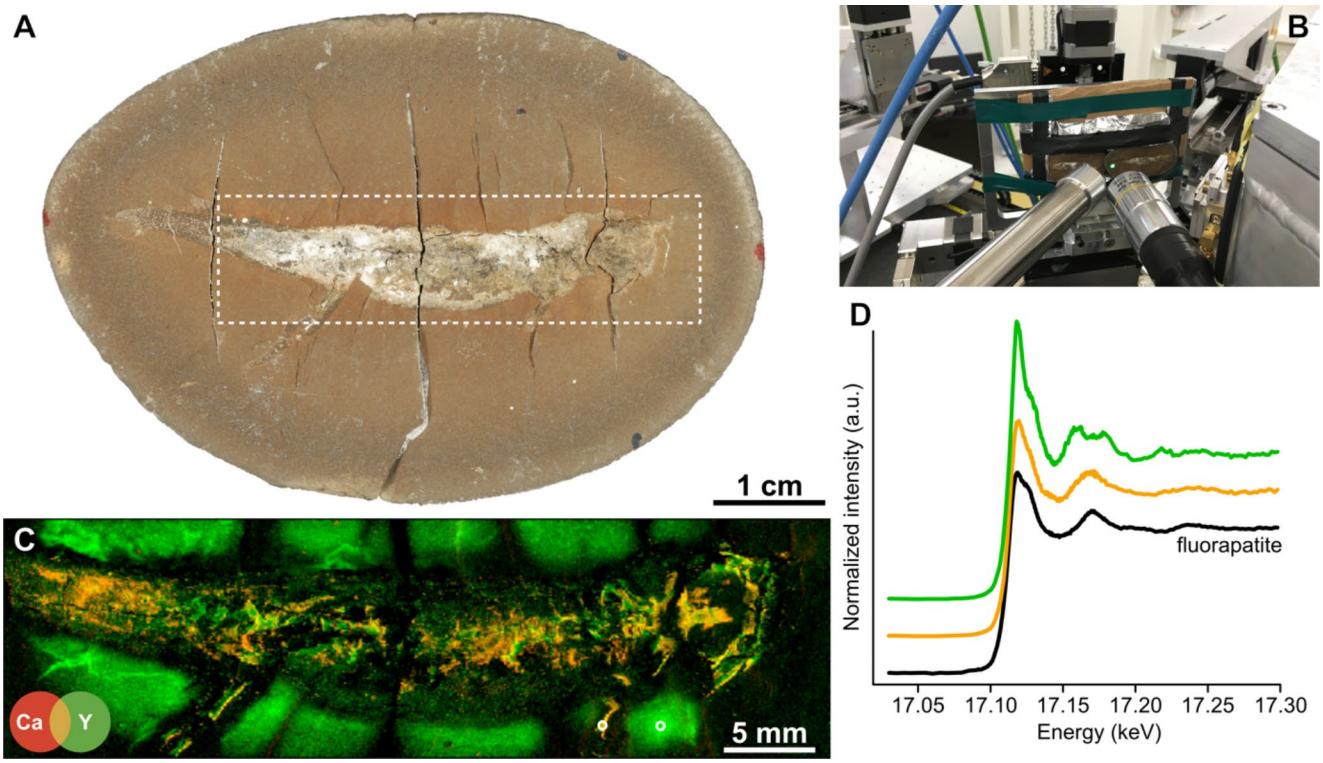

Fig. 6 XRF mapping and XAS spectroscopy of a branchiosaurid amphibian from the Late Carboniferous (ca. -300 Myr) of Montceau-les-Mines, France. A, Optical photograph of the specimen. B, Photograph of the experimental setup, illustrating the use of the larger scanning stages. C, False colour overlay of calcium (red) and yttrium (green) XRF elemental distributions. D, Y K-edge XAS spectra from the right humerus (orange), nearby yttrium hallo (green) and a fluorapatite standard (black). Main acquisition parameters: mapping energy 18 keV, monochromatic; beam size (V x H) ~ 5 µm × 10 µm

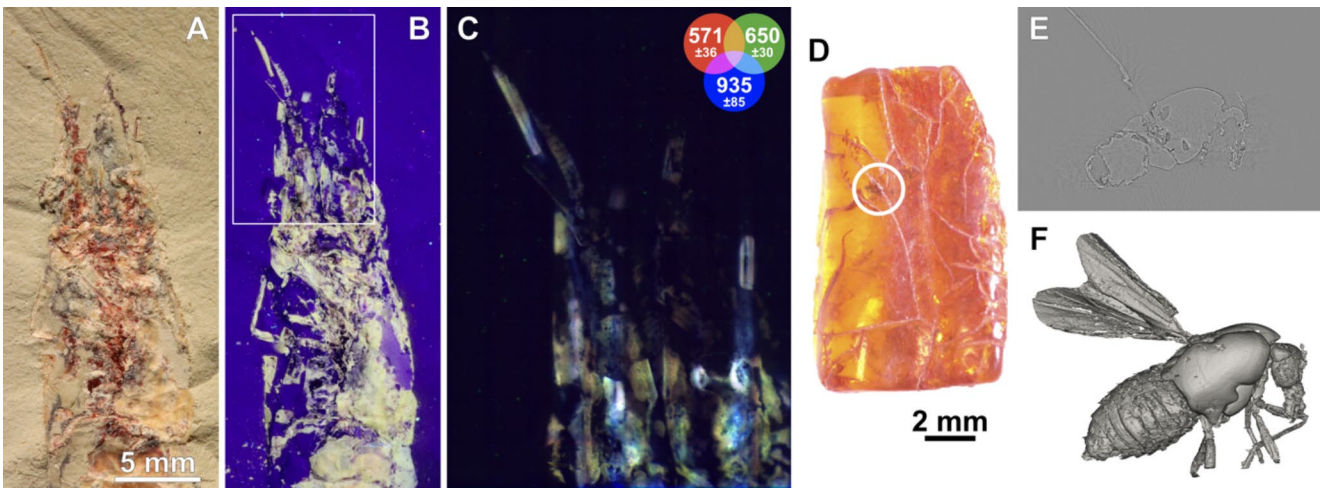

Fig. 7 Paleontological applications under development at the PUMA beamline. A–C, XEOL imaging of a shrimp from the mid-Cretaceous (ca. -100 Myr) of Jbel oum Tkout, Morocco. A, Optical photograph of the specimen. B, UV photograph. C, RGB false colour overlay of XEOL emissions in the yellow (red), red (green) and near infrared (blue) domains, from the box area in B (70 tiles). D–F, X-ray microtomography of an insect trapped in Eocene (ca. -45 Myr) Baltic amber from Poland. D, Optical photograph of the amber piece, with the trapped insect highlighted by the white circle. E, tomogram through the insect. F, Quick 3D rendering of the insect. Main acquisition parameters: energy 12.5 keV (C) and 18 keV (E), all monochromatic; beam size (V x H) ~ 2 mm × 2mm (C) and ~ 20 mm × 5 mm (E, 550 nm voxel size)

take place in 2028 with a shutdown of the facility for 18 months.

For PUMA, our goal will be to offer users a microbeam of 1 μm^2 with a flux several times higher than before the shutdown. The installation of an optimized insertion device should allow us to reach an order of magnitude more flux than pre-upgrade with the U20 undulator, for a total gain in performance of two orders of magnitude compared to current conditions.

Acknowledgements The authors kindly thank all SOLEIL staff who contributed in the planning, construction, and operation of the beamline, as well as all users, who have submitted projects and performed experiments. The PUMA beamline was funded by the 2007–2013 CPER grant IPANEMA of the French Ministry of Research and the Île-de-France Region. The authors thank Ilona Bertrand for the design of the figure of the optical schema of the beamline. CI and LB thank C. Moulherat for access to the material from the Creney-le-Paradis site. PG thanks D. Chabard, A. Medina and S. Charbonnier for the loan of the branchiosaurid amphibian, participants in the fieldwork at the Jbel oum Tkout locality, A. Górski for providing the amber specimen, and A. Favrot for assistance during the X-ray microtomography acquisition presented in Fig. 7.

Author contributions The technical design of the beamline was carried out by S.S., T.M., S.C. and F.B., based on a conceptual design prepared by S.S., S.C. and L.B. S.S., K.M., L.T., A.R., E.B., T.O., M.T. and S.C. contributed to the continuous development of the beamline. S.S., K.M., L.T., A.R., E.B. and T.O performed user support at PUMA. S.S., K.M., L.T., P.G., M.T., E.B., T.O., F.B., C.I., S.C. and L.B. carried out the experiments described. C.I., L.B. and L.R. analyzed and interpreted the results of the textile experiment presented in Sect. 3.2.2. P.G. designed and carried out the experiments, and analyzed and interpreted the results described in Sect. 3.2.3. S.S., K.M., L.T., P.G. C.I., S.C., L.R. and L.B. drafted the manuscript. All authors have read and approved the final version of the manuscript.

Data availability The previously unpublished datasets presented in this paper are available from the corresponding authors on reasonable request.

Declarations

Conflict of interest The authors declare that they have no conflicting interests that could influence the works reported in this publication.

References

1. L. Bertrand, M. Cotte, M. Stampanoni, M. Thoury, F. Marone, S. Schöder, Phys. Rep. **519**, 51 (2012)
2. L. Bertrand, In Trends of Synchrotron Radiation Applications in Cultural Heritage, Forensics and Materials Science. Proceedings of a Technical Meeting held in Vienna, Austria 17—21 October 2011, volume 1803 of TecDoc, pages 48–59. International Atomic Energy Agency, 2016
3. P. Tafforeau, R. Boistel, E. Boller, A. Bravin, M. Brunet et al., Appl. Phys. A-mater. **83**, 195–202 (2006)
4. U. Bergmann, R.W. Morton, P.L. Manning et al., Proc. Natl. Acad. Sci. U S A 107, 9060 (2010)
5. U. Bergmann, P.L. Manning, R.A. Wogelius, Annu. Rev. Anal. Chem. **5**, 361–389 (2012)
6. R.A. Wogelius, P.L. Manning, H.E. Barden et al., Science. **333**, 1622–1626 (2011)
7. P. Gueriau, C. Mocuta, D.B. Dutheil, S.X. Cohen, D. Thiaudière, the OT1 Consortium, S. Charbonnier, G. Clément, L Bertrand, PLoS One. **9**, e86946 (2014)
8. P. Gueriau, C. Mocuta, L. Bertrand, Anal. Chem. **87**, 8827–8836 (2015)
9. P. Gueriau, S. Bernard, L. Bertrand, Elements. **12**, 45–50 (2016)
10. P. Gueriau, S. Réguer, N. Leclercq et al., J. R Soc. Interface. **17**, 20200216 (2020)
11. P. Gueriau, J.-P. Rueff, S. Bernard et al., Anal. Chem. **89**, 10819–10826 (2017)
12. R. Georgiou, P. Gueriau, C. Sahle, S. Bernard, A. Mirone, R. Garrouste, U. Bergmann, J.-P. Rueff, L Bertrand Sci. Adv. **5**, eaaw5019 (2019)
13. L. Bertrand, M.-A. Languille, S.X. Cohen, L. Robinet, C. Gervais, S. Leroy, D. Bernard, E. Le Pennec, W. Josse, J. Doucet, S. Schöder, J. Synchrotron Radiat. **18**, 765 (2011)
14. L. Bertrand, M. Thoury, P. Gueriau, E. Anheim, S. Cohen, Acc. Chem. Res. **54**, 2823–2832 (2021)
15. S.X. Cohen, S.M. Webb, P. Gueriau et al., J. Synchrotron Rad. **27**, 1049–1058 (2020)
16. N. Leclercq, J. Berthault, F. Langlois et al., ICALEPCS., 2015, 15th Int. Conf. on Accelerator and Large Experimental Control Systems, Melbourne, Australia, 17–23 (2015)
17. L. Darricau, A. Mangeret, J. Gorny, E. Joussein, S. Schoeder, J.-L. Reyss, A. Thouvenot, A. Courtin, Appl. Geochem. **167**, 105995 (2024)
18. C. Mongioví, X. Gabrion, J. Govilas, W. Akleh, M. Scheel, J. Perrin, T. Weitkamp, S. Durand, L. Brionne, C. Rivard, S. Schöder, K. Müller, J. Beaugrand, V. Placet, G. Crini, Cellulose (2023)
19. P. Tack, B. Bazi, B. Vekemans, T. Okbinoglu, F. Van Maldeghem, S. Goderis, S. Schöder, L. Vincze, J. synchrotron radiat. **26**, 2033 (2019)
20. F.J. Iguaz, L. Bombelli, S. Meo, F. Orsini, S. Schöder, A. Tocchio, N. Trcera, D. Vantelon, J. Inst. **18**, T06011 (2023)
21. A. Gianoncelli, S. Raneri, S. Schoeder, T. Okbinoglu, G. Barone, A. Santostefano, P. Mazzoleni, Microchem J. **154**, 104629 (2020)
22. A. Gianoncelli, S. Schöder, J.R. Plaisier, M. Fugazzotto, G. Barone, A. Russo, P. Mazzoleni, S. Raneri, Heritage. **7**, 2118 (2024)
23. J. Tapia, M. Eveno, P. Arias, R. Ontañón, S. Schöder, K. Müller, I. Reiche, J. Cult. Herit. **67**, 385 (2024)
24. J. Tapia et al., *Submitted to Applied Physics A*
25. I. Reiche, J. Tapia Reguera, A. Trosseau, Y. Coquinot, A. Maigret, K. Müller, L. Tranchant, S. Schoeder, C. Cretin, archeosciences 93 (2023)
26. T. Moutsiou, D. Ioannides, A. Charalambous, S. Schöder, S.M. Webb, M. Thoury, V. Kassianidou, Z. Zomeni, C. Reepmeyer, Heritage 14 (2022)

27. P.L. Manning, N.P. Edwards, U. Bergmann et al., Nat. commun. **10**, 1–13 (2019)
28. T. Miyashita, M.I. Coates, R. Farrar et al., Proc. Natl. Acad. Sci. U S A, 116, 2146–2151 (2019)
29. P. Gueriau, C. Jauvion, M. Mocuta, Palaeontology. **61**, 981–990 (2018)
30. A. Brayard, P. Gueriau, M. Thoury et al., Geobios. **54**, 71–79 (2019)
31. L. Laibl, H.B. Drage, F. Pérez-Peris, S. Schöder, F. Saleh, A.C. Daley, Geobios. S0016699523000700 (2023)
32. F. Saleh, L. Lustri, P. Gueriau, G.J.-M. Potin, F. Pérez-Peris, L. Laibl, V. Jamart, A. Vite, J.B. Antcliffe, A.C. Daley, M. Nohejlová, C. Dupichaud, S. Schöder, E. Bérard, S. Lynch, H.B. Drage, R. Vaucher, M. Vidal, E. Monceret, S. Monceret, B. Lefebvre, Nat. Ecol. Evol. (2024)
33. T. Saucède, C. Smith, N. Olivier, C. Durlet, P. Gueriau, M. Thoury, E. Fara, G. Escarguel, A. Brayard, Acta Palaeontol. Pol. **68**, (2023)
34. M. Eveno, E. Ravaud, Eur. Phys. J. Plus. **136**, 685 (2021)
35. C. De Mecquenem, M. Eveno, M. Alfeld, R. Pillay, E. Laval, E. Ravaud, I. Reiche, Eur. Phys. J. Plus. **138**, 185 (2023)
36. E. Avranovich Clerici, S. De Meyer, F. Vanmeert, S. Legrand, L. Monico, C. Miliani, K. Janssens, Molecules. **28**, 6106 (2023)
37. L. Bertrand, S. Schöder, D. Anglos, M.B.H. Breese, K. Janssens, M. Moini, A. Simon, TRAC-Trend Anal. Chem. **66**, 128 (2015)
38. L. Bertrand, S. Schöder, I. Joosten, S.M. Webb, M. Thoury, T. Calligaro, É. Anheim, A. Simon, TRAC-Trend Anal. Chem. **164**, 117078 (2023)
39. A. Gimat, S. Schöder, M. Thoury, M. Missori, S. Paris-Lacombe, A.-L. Dupont, Biomacromolecules. **21**, 2795 (2020)
40. A. Gimat, S. Schöder, M. Thoury, A.-L. Dupont, Cellulose. **29**, 4347 (2022)
41. M. Godet, L. Binet, S. Schöder, L. Brunel-Duverger, M. Thoury, L. Bertrand, J. Anal. Spectrom. **37**, 1265 (2022)
42. N.J. Conard, Nature. **426**, 830–832 (2003)
43. N.J. Conard, M. Malina, S.C. Münzel, Nature. **460**, 737–740 (2009)
44. N.J. Conard, Musée national de la préhistoire, pp. 13–16 (2018)
45. I. Reiche, C. Heckel, K. Müller, O. Jöris, T. Matthies, N.J. Conard, H. Floss, R. White, Angew Chem. Int. Ed. **57**, 7428–7432 (2018)
46. L. Tranchant, K. Müller, Q. Lemasson, L. Pichon, S. Schöder, N.J. Conard, I. Reiche, Nucl. Instrum. Meth B **545**, 165146 (2023)
47. L. Tranchant, K. Müller, Q. Lemasson, L. Pichon, S. Schöder, N. Conard, I. Reiche, Quatern Int. **660**, 4–12 (2023)
48. E. Chalmin, *PhD thesis*, Université de Marne la Vallée, 2003
49. P. Goldberg, S. Schiegl, K. Meligne, C. Dayton, N.J. Conard, E&G Quatern. Sci. J 53, 1–25 (2003)
50. I.-M. Zougrou, M. Katsikini, M. Brzhezinskaya, F. Pinakidou, L. Papadopoulou, E. Tsoukala, E. Paloura, Sci. Nat-Heidelberg. **103**, 1–12 (2016)
51. C. Iacconi, A. Autret, E. Desplanques, A. Chave, A. King, B. Fayard, C. Moulherat, E. Leccia, L. Bertrand, J. Archaeol. Sci. **149**, 105686 (2023)
52. C. Iacconi, E. Desplanques, C. Moulherat, M. L'Héronde, A. King, A. Autret, S. Schoeder, B. Fayard, E. Leccia, L. Bertrand, Antiquity (in press). https://doi.org/10.15184/aqy.2024.96
53. C. Biagioni, L.L. George, N.J. Cook, E. Makovicky et al., 105, 109–122 (2020)
54. C. Biagioni, J. Sejkora, Y. Moëlo, Y et al Mineralogical Magazine. **86**, 331–339 (2022). https://doi.org/10.1180/mgm.2022.26)
55. P. Gueriau, S. Bernard, F. Farges et al., Geology. **48**, 1164–1168 (2020)
56. V.L. Coli, L. Gomart, D.F. Pisani, S.X. Cohen, L. Blanc-Féraud, J. Leblond, D. Binder, Archaeometry. **64**, 84 (2022)
57. J. Susini, J.M. Cassagne, B. Gagey et al., Eur. Phys. J. Plus. **139**, 80 (2024). https://doi.org/10.1140/epjp/s13360-024-04872-2